Article

Compressed orthogonal coded Multiplexing Wide-band Millimeter Wave Imaging - A Numerical Study

Hao Tu , Xiangxin Meng, Taorong Liu, Hui Feng and Shuai Wu *

Brainware Terahertz Information Technology Co. Ltd., Hefei 230001, China; dragontuhao@163.com (H.T.); 15856969462@163.com (X.M.); 1938837635@qq.com (T.L.); 15855174276@163.com (H.F.); shuaiwu52@126.com (S.W.)

* Correspondence: shuaiwu52@126.com; Tel.: +86-551-6573-6511

Abstract: Millimeter wave wide-band imaging is widely studied for a variety of applications. However real-time millimeter wave wide-band imaging at frequencies above 30GHz for moving targets in a large field of view has not been realized commercially. A 2D sparse array with transmitter multiplexing is a promising solution to this problem. In this article, a method combining compressed sensing and orthogonal coded multiplexing was proposed, and the imaging performance was analyzed for different reconstruction algorithms and observation matrices by imaging simulation for a continuous object. Also the influence on the dynamic range of the original signal introduced by orthogonal coded multiplexing was studied. This work demonstrated that the proposed method was effective in reconstructing the image with a real-time capability. It is shown that different algorithms and matrices resulted in distinct performances, while the evaluation parameter selection also played a role. This work provided useful instructions for both the hardware and software design of a real-time 3D millimeter wave imaging system in the future.

Keywords: millimeter wave imaging; orthogonal coded multiplexing; compressed sensing; real-time imaging; dynamic range

---

1. Introduction

Millimeter wave (MMW) imaging has attracted a lot of attention recently, due to its potential applications in personnel screening[1,2], industrial quality inspection[3,4], and medical imaging[5,6] etc. The advantages of MMW imaging compared to some of the traditional methods include the following. (1) No ionizing radiation is involved compared to X-ray imaging, making it safe for personnel imaging. (2) It can penetrate through many dielectric substances, enabling its application for hidden item identification and industrial inspection. (3) It is sensitive to water molecules so that pathological changes can be distinguished from healthy tissues. (4) The imaging resolution can reach millimeter level which is adequate for small item inspection. (5) Devices are more mature than those in the terahertz band, which makes it more competent from the commercial point of view.

In many of the afore-mentioned real-life scenarios, such as security screening, real-time imaging for moving targets and high resolution are required simultaneously. The solution to satisfy both the requirements is adopting transmitter or receiver arrays. Pacific Northwest National Laboratory has developed a linear antenna array around 30GHz, which is commercially used in the L3 ProVision system for airport security check-points[2]. Fraunhofer Institute has adopted a W band linear array for quality inspection[7]. These systems using linear array either mechanically scan the field of view, or require the target to move on a conveyor belt, thus they are not able to image the field of view (FoV) with a real-time frame rate. Johann Wolfgang Goethe-University proposed to combine a terahertz linear array with a rotating trigonal mirror to realize real-time personnel screening[8]. But in the dimension parallel to the array, a real aperture had to be formed which resulted in worse image quality and severe specular reflection effect.

Aimed at solving real-time 3D MMW imaging problem, a lot of researches has focused on using 2D sparse arrays to substitute 1D linear arrays where the sampling speed can be increased by an order of magnitude. Rohde and Schwarz developed a 2D sparse array system at E-band for security check-points, which can realize a sampling speed of 16ms[9]. But according to the criterion that the imaged object should move less than a quarter of the wavelength during the sampling time, this speed is still not fast enough to image a walking person. MIT Lincoln Laboratory made a real-time sparse array system by using phase center approximation to divide the array into smaller regions where coherent accumulation was performed[10]. Although it reached a frame rate of 10Hz, the approximation introduced severe image degradation at near range. Currently, there is no reported system that can have a millimeter level resolution and a moving-target image capability, together with a robust algorithm that brought no obvious quality degradation at all distances. The main problem is that most of the systems used a time division multiplexing technology in which the transmitters are electronically switched. This switching process is time-consuming, especially for the high resolution systems at higher frequency band with more transmitter elements, preventing the system to image moving objects.

Frequency or orthogonal coded multiplexing (OCM) technology can be used to eliminate the switching process[11,12]. However, frequency multiplexing raises strict demands for low phase noise and wide sampling bandwidth, both difficult to realize and increase system cost. On the other hand, OCM replaces the switching between elements to switching between codes, as demonstrated by University of Washington and Duke University. If the switch times of the two processes are the same, then no reduction in sampling time is realized because the length of the code should be no less than the number of the transmitters.

Aiming at real-time high-resolution millimeter wave imaging for security applications, we propose and study a new method in this work, where OCM is combined with compressed sensing (CS)[13], so that the code length is reduced and the sampling time is shortened. We analyze the influence of different choices of reconstruction algorithms and observation matrices on the imaging quality by using peak signal-to-noise ratio (PSNR) and image entropy as evaluation criteria. Imaging under noisy environment is also simulated, which demonstrates that the proposed method works better compared to time division multiplexing method when signal-to-noise ratio is low. We also analyze the statistics of the echo signal at the receiver channels and discuss the influences on the receiver channels. The results of this work provide some insights for the future design of a high resolution MMW imaging system with real-time capability for moving targets by using OCM technology.

This article is organized as follows. Section 2 introduces the theoretical model of the imaging process with OCM and CS. Simulation results of the imaging quality for a continuous object are displayed and analyzed for different algorithms and noise levels in Section 3. Signal statistical characteristics is studied in Section 4. Section 5 concludes this work.

2. Imaging Model of OCM with CS

The imaging model discussed here is schemed in Figure 1 for a sparse array configuration. The transmitters simultaneously transmit millimeter wave signals to the target area while the back-scattered waves are detected by the receivers working in parallel. To distinguish signals coming from distinct transmitters at a single receiver, the transmitted signals need to be coded where the code sequences for different transmitters are orthogonal.

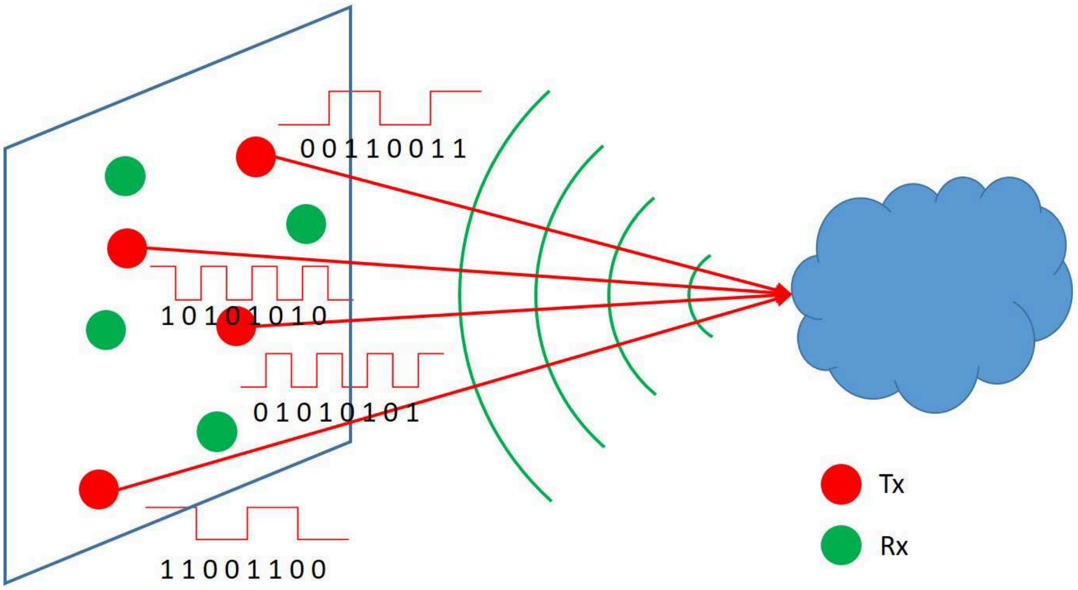

Figure 1. A scheme diagram for the imaging process of OCM.

For simplicity, we discuss the situation where a single frequency is used here, and the results can be easily extended to the wide-band case. The echo signal $S_n(t)$ at the n-th receiver is expressed as

$$S_n(t) = \sum_m C_m(t) \int\int\int f(x,y,z) \exp[-jk(D_m + D_n)]dxdydz \tag{1}$$

where t denotes the slow time indexing the code sequences, $C_m(t)$ is the code sequence for the m-th transmitter, $f(x,y,z)$ is the complex scatter coefficient at location (x,y,z), k is the wave vector, and D_m and D_n are the distances from (x,y,z) to the transmitter and receiver, respectively. By discretizing the target area into a set of voxels, Equation (1) can be written as

$$S_n(t) = \sum_{m,i} C_m(t) \exp[-jk(D_m + D_n)] f_i \tag{2}$$

where i is the index for the voxels. It is easily seen that it can be further written in a matrix form as

$$Sn = \Phi_n F \tag{3}$$

where Sn is a $L \times 1$ vector with L denotes the code length, F is a $P \times 1$ vector with P denotes the number of voxels to be imaged, and Φ is the measurement matrix with dimension $L \times P$ whose elements are expressed as

$$\Phi_{lp} = \sum_m c_m(l) \exp[-jk(D_{mp} + D_{np})] \tag{4}$$

When the signals for different receivers are combined together, the vector Sn is expanded to length $L \times N$ and the measurement matrix Φ is expanded to $LN \times P$, where N is the total number of receivers. In many imaging scenarios, LN is much less than P, so Equation (4) becomes a compressive sensing problem. However the matrix Φ is usually so large that common compressive sensing solvers can hardly give robust reconstruction results in a reasonable computation time.

To reduce the computation load, the imaging problem can be decomposed into two steps. The echo signal S_{mn} for the m-th transmitter is decomposed from $S_n(t)$ in the first step. To do this, Equation (2) can be rewritten as

$$S_n(t) = \sum_m C_m(t) S_{mn} \tag{5}$$

where

$$S_{mn} = \sum_{i} \exp[-jk(D_m + D_n)] f_i \tag{6}$$

Thus Equation (5) itself now is a compressive sensing problem when the code length L is smaller than the number of transmitters M, and S_{mn} can be computed from readily available algorithms with a reduced complexity. Then, in the second step, the well-known back-projection (BP) algorithm can be applied to reconstruct the image with

$$f_i = \sum_{m,n} \exp[jk(D_m + D_n)] S_{mn} \tag{7}$$

When a wide-band system is involved, we can obtain the 1D image in the depth-direction for each transmitter-receiver pair by using pulse compression technique, and then apply the BP process[14,15] with an interpolation of the 1D image to a rectangular grid. In the next section, we will analyze the influences to the imaging result of different CS algorithms and measurement matrices following the imaging process described by Equations (5)-(7).

3. Simulation results

A rectangular-shaped sparse array configuration was used for the simulation as chosen in Reference [9]. The array consisted of 94 transmitters and 94 receivers as shown in Figure 2. The working band was chosen as 30-36GHz with 40 frequency steps. To better evaluate the performance of the proposed method, the imaging target was chosen to be three continuous objects in the shape of capital letters 'T', 'H' and 'Z' as shown in Figure 3, rather than point targets. The targets were composed of fully conductive materials and placed at a distance of 0.2m from the array.

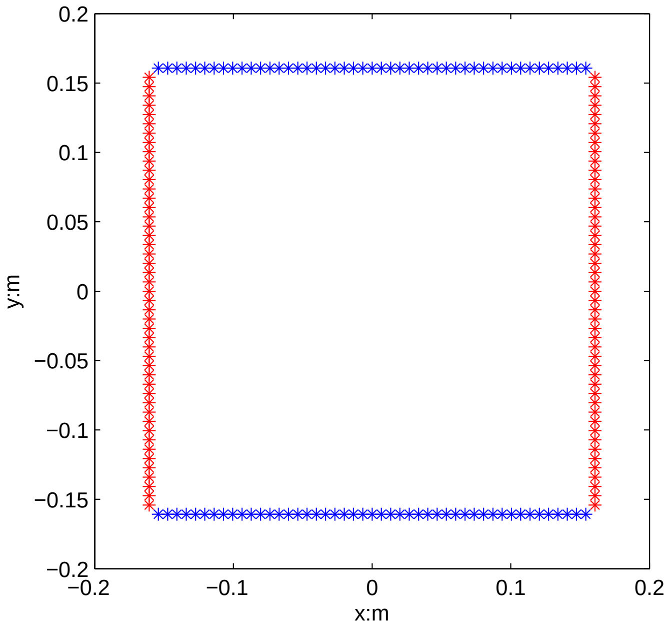

Figure 2. The sparse array used in the simulation. The red asteroids denote the positions of the transmitter elements while the blue ones denote the positions of the receiver elements.

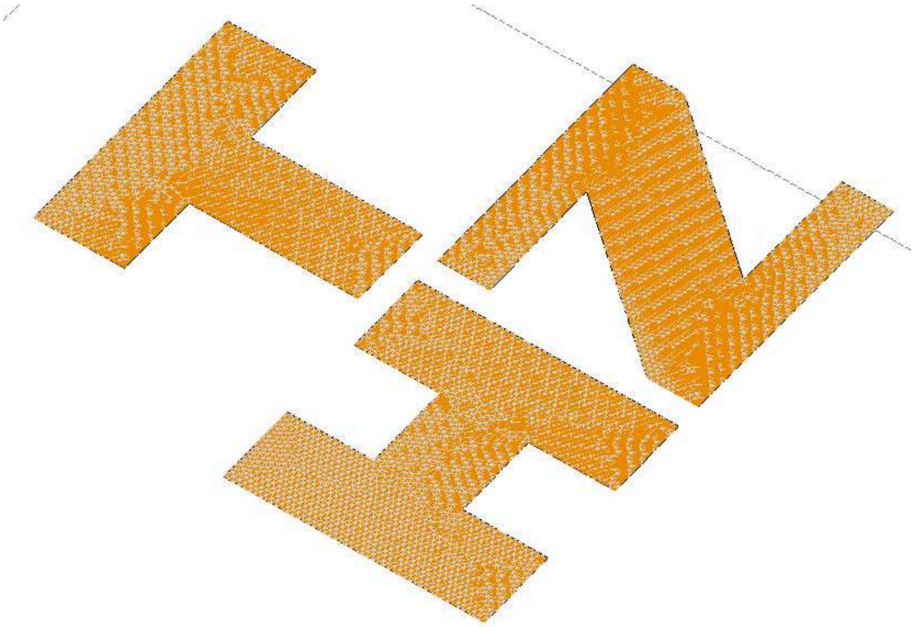

Figure 3. The continuous target with the shapes of capital letters 'T', 'H' and 'Z' used in the simulation.

Two parameters were used to judge the reconstruction quality. The first was the peak signal-to-noise ratio (PSNR) defined as in Reference [16] which is expressed as

$$PSNR = 10\log_{10} \left. \frac{\max(F)^2}{\frac{1}{P}\sum_{i=1}^{P}(F-\hat{F})^2} \right) \tag{8}$$

where F represents the true solution of the target which is calculated for a non-compressive case, and $\hat{F}$ is the reconstructed image. The second parameters was the two-dimensional image entropy, defined as

$$H = -\sum_{i=0}^{255}\sum_{j=0}^{255} P_{ij} \ln P_{ij} \tag{9}$$

where H is the 2D image entropy, and P_{ij} is a probability distribution function defined as the probability that a pixel's gray-scale value is i and the same pixel's gray-scale value in an average-filtered image is j. PSNR describes the deviation of the reconstructed image from the true solution, which should be as large as possible. Image entropy describes the information contained in the reconstructed image, or in other words, the level of order in the image, where a smaller value denotes a better image quality. Imaging result from a time-division multiplexing method is used as the ground truth, as shown in Figure 4.

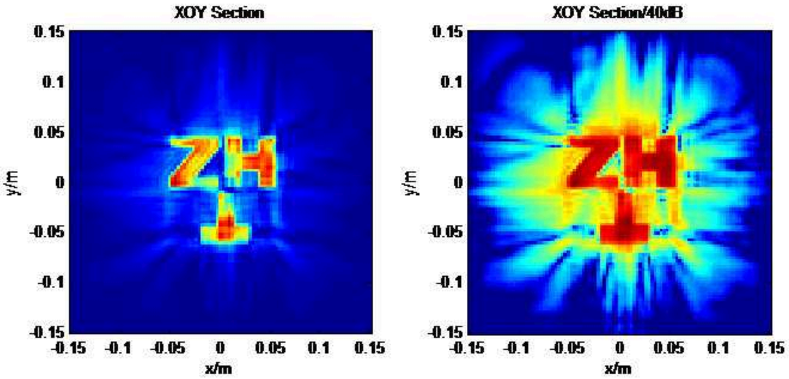

Figure 4. Reconstruction results under time-multiplexing mode, working as the ground truth of the target.

There are many readily available CS algorithms to solve Equation (5)[17–19]. According to the fact that the target information is unknown before the reconstruction, algorithms without requirements of a-priori knowledge of the imaged scene are chosen. Three reconstruction algorithms were tested in our simulation, namely the SLIM algorithm[20], the TVAL3 algorithm[21] and the Hadamard relaxation method[22]. These algorithms were chosen due to their high computation efficiency, especially the latter two, which is meaningful for real-time imaging applications. Also, different choices of measurement matrix C_m were tested including standard Hadamard matrix, Hadamard matrix generated from twin prime method[22], random matrix, and random Bernoulli matrix.

First, imaging under ideal conditions with no noise present was simulated. Figure 5, Figure 6 and Figure 7 display the imaging results of the Hadamard relaxation method, the SLIM algorithm and the TVAL3 algorithm at 50% under-sampling ratio for different measurement matrices, respectively, while we point out that the computation process failed to converge when the SLIM method was used with the standard Hadamard matrix as the measurement matrix. Note that due to the restriction of the Hadamard relaxation method, the matrices generated for this method had a dimension of 143 × 143, while the other matrices had dimensions of 94 × 94.

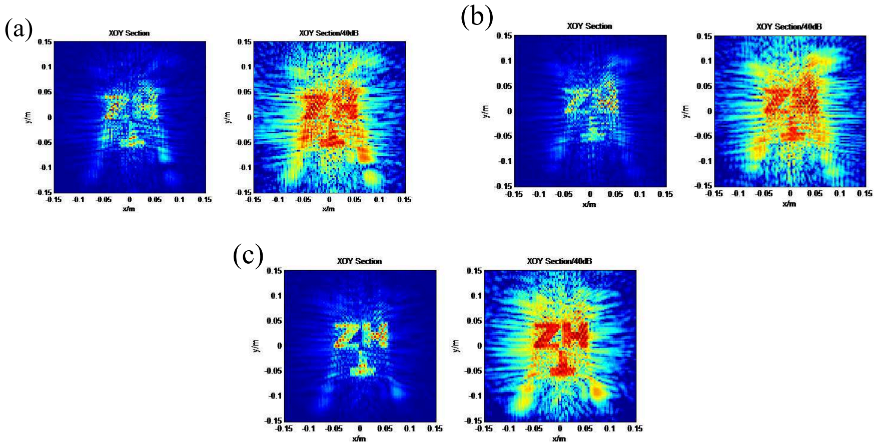

Figure 5. Reconstruction results of the Hadamard relaxation method at 50% under-sampling ratio for measurement matrices of (a) random Bernoulli matrix, (b) random matrix, (c) Hadamard matrix generated by the twin-prime method. In each of the sub-image, the magnitude is shown in a linear-scale on the left side, and in a logarithmic-scale on the right side with a 40-dB dynamic range.

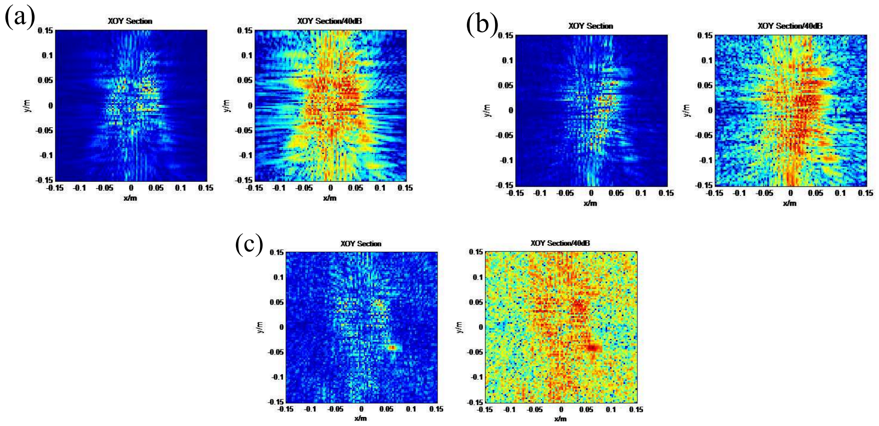

Figure 6. Reconstruction results of the SLIM algorithm at 50% under-sampling ratio for measurement matrices of (a) random Bernoulli matrix, (b) random matrix, (c) Hadamard matrix generated by the twin-prime method. In each of the sub-image, the magnitude is shown in a linear-scale on the left side, and in a logarithmic-scale on the right side with a 40-dB dynamic range.

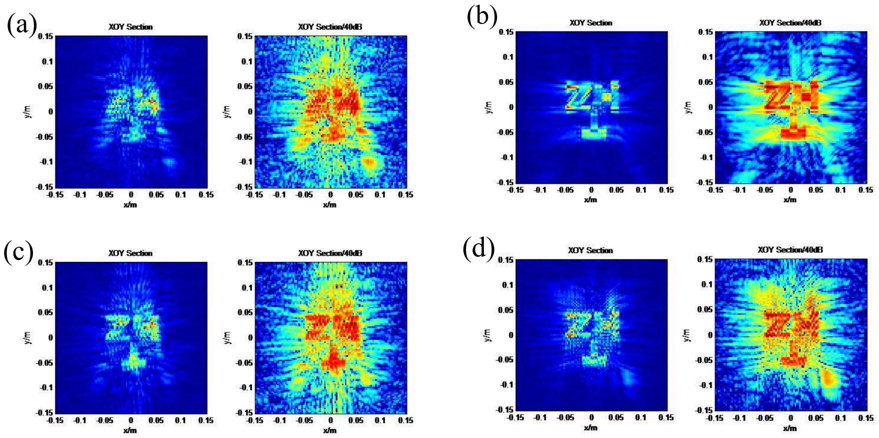

Figure 7. Reconstruction results of the TVAL3 algorithm at 50% under-sampling ratio for measurement matrices of (a) random Bernoulli matrix, (b) standard Hadamard matrix, (c) random matrix, (d) Hadamard matrix generated by the twin-prime method. In each of the sub-image, the magnitude is shown in a linear-scale on the left side, and in a logarithmic-scale on the right side with a 40-dB dynamic range.

From Figure 5 to Figure 7, it can be seen that the SLIM method generated the worse reconstruction results where the shapes of the letters were indiscernible, while the other two algorithms could successfully reconstruct the images containing the three letters, so the SLIM method is dropped for the following discussions. The image qualities of these images were obviously degraded caused by the down-sampling, compared to the ground truth shown in Figure 4. Two of these images looked best with the clearest boundary of the letters and lowest background noises. These two were generated from the combination of the Hadamard relaxation method with the twin-prime Hadamard matrix (referred to as Rlx+Twin method in the following), and the TVAL3 algorithm with the standard Hadamard matrix (referred to as TVAL3+Had method in the following), respectively. To quantitatively evaluate the performance of these methods, the PSNR and image entropy are plotted in Figure 8 for down-sampling ratio from 10% to 90%. It is demonstrated in Figure 8 that the Rlx+Twin method has the highest PSNR and the TVAL3+Had method has the lowest image entropy. This result is consistent with the conclusion reached by visual inspection that these two methods give the best imaging result. However these two evaluation criterion give distinct results, meaning that the method with the lowest entropy does not have the highest PSNR, and vice versa. This might be due to the different aspects concerned by the two parameters, where PSNR describes the maximum deviation from the ground truth and the image entropy focuses on the amount of information contained in an image.

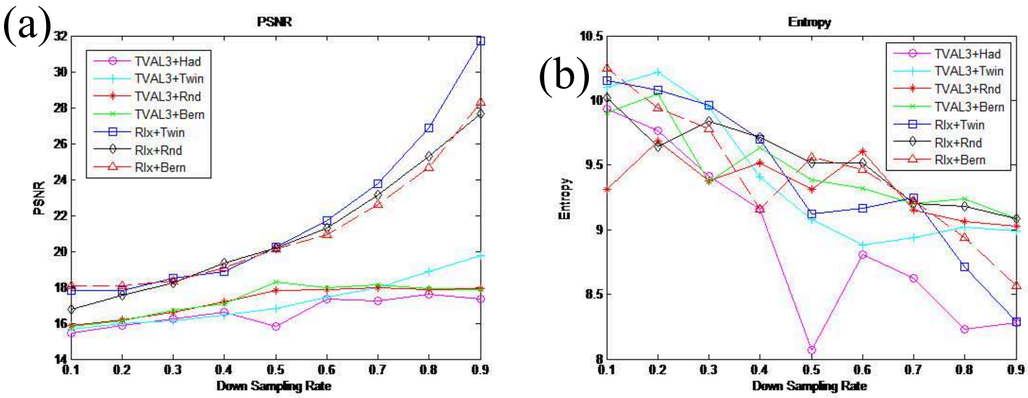

Figure 8. (a) PSNR for different combinations of CS algorithms and measurement matrices as a function of down-sampling rate. (b) Image entropy for different combinations of CS algorithms and measurement matrices as a function of down-sampling rate.

To demonstrate the robustness of the Rlx+Twin method and the TVAL3+Had method, we added random Gaussian noises to the original signals and reconstructed the images with the two methods. The signal-to-noise ratio (SNR) is defined as the magnitude of the additive noise to the maximum signal acquired during a time-division multiplexing sampling where no OCM is applied. And the under-sampling ratio was set to 50%. Reconstruction results are displayed in Figure 9 to Figure 11 for SNR of 10dB, 0dB and -10dB, respectively, where the results for time-division multiplexing are also shown as a comparison.

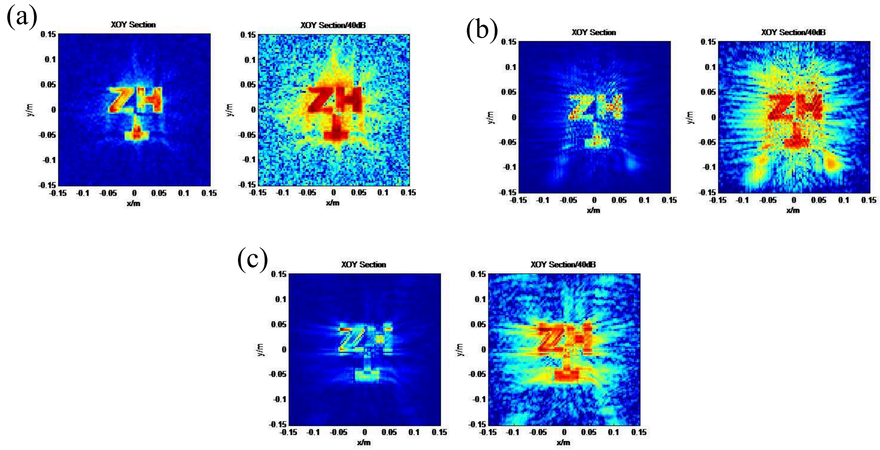

Figure 9. Reconstruction results under SNR=10dB for (a) time-division multiplexing, (b) Rlx+Twin method, (c) TVAL3+Had method. In each of the sub-image, the magnitude is shown in a linear-scale on the left side, and in a logarithmic-scale on the right side with a 40-dB dynamic range.

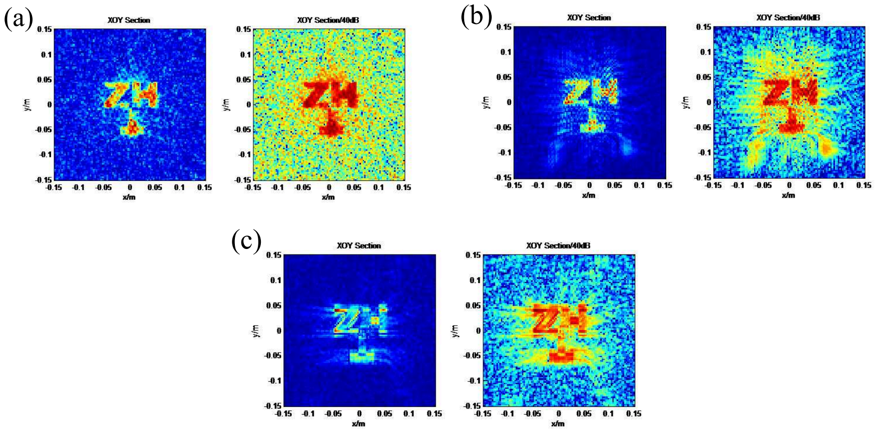

Figure 10. Reconstruction results under SNR=0dB for (a) time-division multiplexing, (b) Rlx+Twin method, (c) TVAL3+Had method. In each of the sub-image, the magnitude is shown in a linear-scale on the left side, and in a logarithmic-scale on the right side with a 40-dB dynamic range.

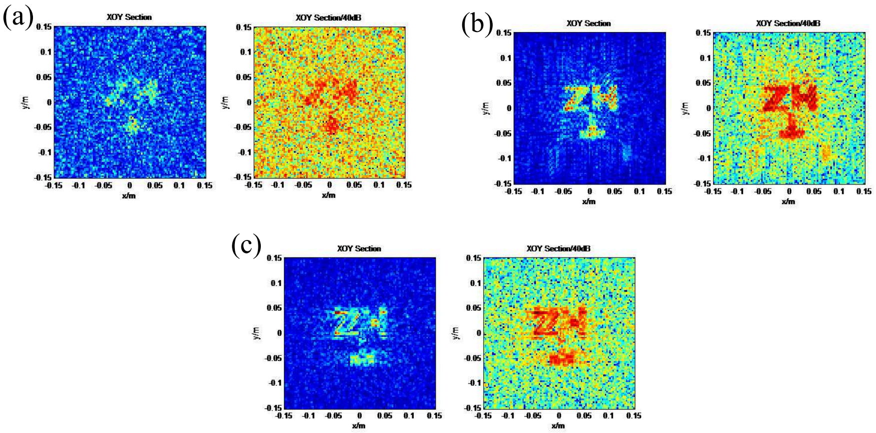

Figure 11. Reconstruction results under SNR=-10dB for (a) time-division multiplexing, (b) Rlx+Twin method, (c) TVAL3+Had method. In each of the sub-image, the magnitude is shown in a linear-scale on the left side, and in a logarithmic-scale on the right side with a 40-dB dynamic range.

From Figure 9-11, it can be seen that the proposed OCM method combined with CS technology can successively reconstruct the targets in noisy conditions. For high SNR cases, all three methods generated good reconstruction quality. But when noise is strong, as in the SNR=-10dB case, TDM failed to produce a clear image of the three letters, while the proposed methods gave better results, especially the Rlx+Twin method, which still produced a clear image of the targets. This result demonstrated the robustness of the Rlx+Twin method and the TVAL3+Had method, and proved that by using OCM with CS, better reconstruction quality could be obtained compared to the traditional TDM methods. In Figure 12, SNR was tuned from -30dB to 40dB, and the PSNR and the image entropy were used to evaluate the performance of the three methods. It is seen that at high SNR, the TDM methods give the best reconstruction quality due to its full sampling. As the SNR lowers, the performances of the three methods became similar. And as the SNR further decreases below 0dB, the Rlx+Twin and TVAL3+Had methods could give better results. Similar to the previous results shown in Figure 8, different evaluation criterion favored different methods for low SNR case between 0dB and -20dB, whereas the Rlx+Twin method generated the highest PSNR, and the TVAL3+Had method reached the lowest entropy. Note that below -20dB SNR all methods failed to reconstruct the targets.

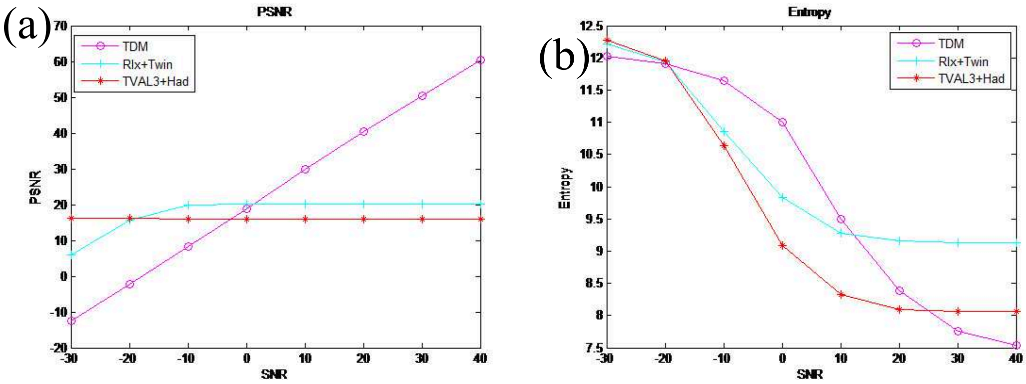

Figure 12. (a) PSNR for TDM, Rlx+Twin method and TVAL3+Had method at different SNR. (b) Image entropy for TDM, Rlx+Twin method and TVAL3+Had method at different SNR.

4. Signal Statistics

In the previous section, the capability of reconstructing images by the proposed method both under ideal and noisy conditions was illustrated. But since OCM method utilizes multiple transmitters simultaneously which may result in strong coherent effects, the magnitude of the received signal may be larger than that in a conventional TDM method. Thus the maximum signal acceptable by the DAQ and also the dynamic range need to be selected carefully according to the signal statistics. So in this section, we briefly display the signal statistics of the TDM, Rlx+Twin and TVAL3+Had method and summarizes the influence brought by applying our proposed method on the receiver channel.

In Figure 13, the power of the simulated signal for TDM, standard Hadamard matrix coded and twin-prime Hadamard matrix coded cases are displayed for the first 1000 points, respectively. It is obvious seen in this figure that by applying OCM method, the power of the back-scattered signal from the targets is largely increased by several octaves, which is further proved by the signal statistics shown in Table 1.

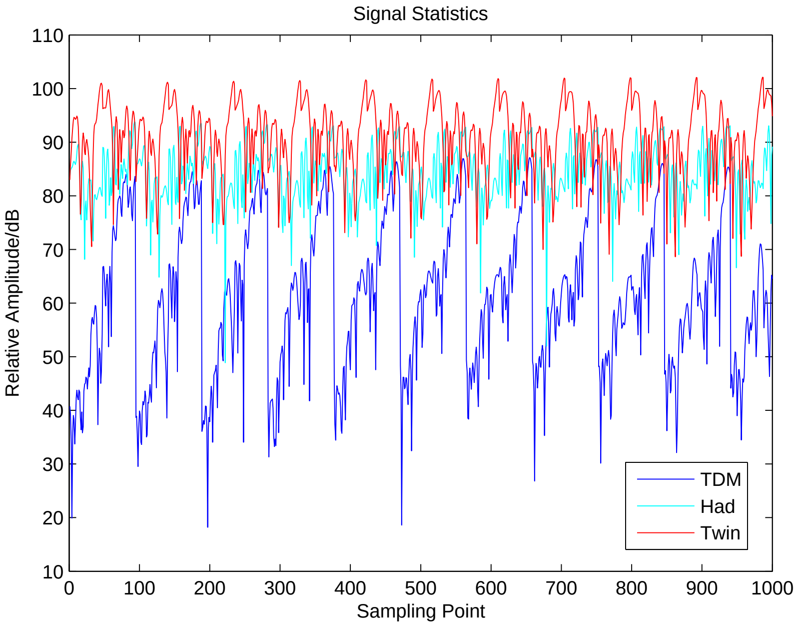

Figure 13. Power of the echo signal for TDM (blue), Hadamard matrix coded (cyan) and twin-prime Hadamard matrix coded (red) cases.

Table 1. Signal statistics for TDM, Hadamard matrix coded and twin-prime Hadamard matrix coded cases.

Method	Maximum	Minimum	Mean	Standard Deviation
TDM	1.031×10^{9}	1.840	3.461×10^{7}	9.560×10^{7}
Twin	6.313×10^{10}	3.860×10^{3}	3.253×10^{9}	4.963×10^{9}
Had	5.999×10^{10}	1.082×10^{3}	3.273×10^{9}	4.212×10^{9}

It is seen from Table 1 that the mean echo signal power is increased by approximately two orders of magnitude when the OCM method is used instead of TDM method. And the maximum echo signal is increased 60 times, which is in accordance with the case of constructive interference for 94 receiver channels, where the signal should be multiplied by 94 times theoretically. This indicates that the compression point of the receiver channel need to be higher for about two octaves when OCM method is used. For the security check application at close range, this can be easily achieved by modern semi-conductor fabrication technologies and analog-to-digital modules (AD). Now we analyze the influence on the dynamic range of the receiver. From the previous section, we can see that the acceptable noise level for OCM can be one order of magnitude higher than for TDM method. Given that the signal is two octaves higher, the dynamic range, which can be represented by the maximum signal divided by the noise level, should be one order of magnitude higher when OCM method is involved. Note that in the current active millimeter-wave body scanners, the dynamic range at the receiver side is usually much higher than 0dB, which is the lowest acceptable level in our simulated results, thus we infer that the OCM method should be applicable without further increase the dynamic range of the receiver channel and the analog-to-digital module.

These analysis verified the applicability of the proposed method from the hardware perspectives.

5. Conclusions

Aiming at high-resolution real time active millimeter wave imaging for security applications, a method combining orthogonal coded multiplexing and compressed sensing was proposed in this work for sparse array configuration. The performance for different CS algorithms and different choices of coding matrices was analyzed and compared to the time division multiplexing method. By visually checking, calculating the PSNR and image entropy, it was found that the Rlx+Twin and TVAL3+Had methods reached the best imaging performance, where Rlx+Twin method was even better for noisy circumstances. Compared to the TDM method, the proposed method was more robust under worse SNR. Also the statistics for the echo signal was studied to prove the feasibility of the method for current available hardware. In the future, the simulations for more complex targets, such as a human body model, should be carried out to further prove the performance of this method. And to build a real system, we still need to construct a computation routine to be effectively executed in a CPU or GPU to realize real-time imaging.

Author Contributions: conceptualization, H.T.; methodology and simulation, H.T. and X.M.; data analysis, H.T.; validation, T.L. and H.F.; supervision, S.W.

Funding: This research received no external funding.

Acknowledgments: We thank Wusheng Yao and Lin Chen for helpful discussions.

Conflicts of Interest: The authors declare no conflict of interest.

References

1. Appleby, R., Anderton R.N. Millimeter-wave and submillimeterwave imaging for security and surveillance. *Proc. IEEE* **2007**, *95*, 1683–1690.
2. Sheen, D.M., McMakin D.L., Hall T.E. Three-dimensional millimeter-wave imaging for concealed weapon detection. *IEEE Trans. Microw. Theory Tech.* **2001**, *49*, 1581–1592.

3. Viegas, C., Alderman, B., Powell, J., Liu, H., Wang, H., Sloan, R. Millimeter wave radiometers for applications in imaging and nondestructive testing. *2015 8th UK, Europe, China Millimeter Waves and THz Technology Workshop (UCMMT)* **2015**, Sep. 2015.
4. Guo, Q., Chang, T., Cui, H. Three-dimensional millimeter wave imaging of borehole wall cracks. *43rd International Conference on Infrared, Millimeter, and Terahertz Waves (IRMMW-THz)* **2018**, Sep. 2018.
5. Gao, Y., Zoughi, R. Millimeter wave reflectometry and imaging for noninvasive diagnosis of skin burn injuries. *IEEE Trans. Instrum. Meas.* **2017**, *66*, 77–84.
6. Oppelt, D., Korf, P., Adametz, J., Groh, J., Vossiek, M., Zhuravleva, K., Goertz, O. Effects of Different Types of Burn Wounds and its Dressings on Millimeter-Wave Images. *Frequenz* **2018**, *72*, 151–158.
7. Baccouche, B., Agostini, P., Mohammadzadeh, S., Kahl, M., Weisenstein, C., Jonuscheit, J., Keil, A., Loeffler, T., Sauer-Greff, W., Urbansky, R., Bolivar, P.H., Friederich, F. Three-Dimensional Terahertz Imaging With Sparse Multistatic Line Arrays. *IEEE Journal of Selected Topics in Quantum Electronics* **2017**, *23*, 8501411.
8. Friederich, F., von Spiegel, W., Bauer, M., Meng, F., Thomson, M.D., Boppel, S., Lisauskas, A., Hils, B., Krozer, V., Keil, A., Loeffler, T., Henneberger, R., Huhn, A.K., Spickermann, G., Bolivar, P.H., Roskos, H.G. THz Active Imaging Systems With Real-Time Capabilities. *IEEE Trans. Terahertz Sci. Tech.* **2011**, *1*, 183–200.
9. Ahmed, S.S., Schiessl, A., Schmidt, L.P. A Novel Fully Electronic Active Real-Time Imager Based on a Planar Multistatic Sparse Array. *IEEE Trans. Microw. Theory Tech.* **2011**, *59*, 3567–3576.
10. Moulder, W.F., Krieger, J.D., Majewski, J.J., Coldwell, C.M., Nguyen, H.T., Maurais-Galejs, D.T., Anderson, T.L., Dufilie, P., Herd, J.S. Development of a High-Throughput Microwave Imaging System for Concealed Weapons Detection. *2016 IEEE International Symposium on Phased Array Systems and Technology(PSAT)* **2016**, Oct. 2016.
11. Koeppel, T., Methfessel, S., Schiessl, A., Schmidt, L.P., Increasing Measurement Speed in mm-Wave Imaging Systems by Means of Frequency Multiplexing. *2013 European Microwave Conference* **2013**, Oct. 2013.
12. Pedross-Engel, A., Arnitz, D., Gollub, J.N., Yurduseven, O., Trofatter, K.P., Imani, M.F., Sleasman, T., Boyarsky, M., Fu, X., Marks, D.L., Smith, D.R., Reynolds, M.S. Orthogonal Coded Active Illumination for Millimeter Wave, Massive-MIMO Computational Imaging with Metasurface Antennas. *IEEE Trans. Computational Imag.* **2018**, *4*, 184–193.
13. Candes, E.J., Romberg, J., Tao, T. Robust Uncertainty Principles: Exact Signal Reconstruction from Highly Incomplete Frequency Information. *IEEE Trans. Inf. Theory* **2006**, *52*, 489–509.
14. Desai M., Jenkins, W. Convolution Backprojection Image Reconstruction for Spotlight Mode Synthetic Aperture Radar. *IEEE Trans. Image Proc.* **1992**, *1*, 505–517.
15. Ulander, L., Hellsten, H., Stenstrom, G. Synthetic-Aperture Radar Processing using Fast Factorized Back-projection. *IEEE Trans. Aerospace Electronic Sys.* **2003**, *39*, 760–776.
16. Zamani, H., Fakharzadeh, M. 1.5-D Sparse Array for Millimeter-Wave Imaging Based on Compressive Sensing Techniques. *IEEE Trans. Antenna Propagation* **2018**, *66*, 2008–2015.
17. Mota, J.F.C., Xavier, J.M.F., Aguiar, P.M.Q., Puschel, M. Distributed Basis Pursuit. *IEEE Trans. Sig. Proc* **2012**, *60*, 1942–1956.
18. Tropp, J.A., Gilbert, A.C. Signal Recovery from Random Measurements via Orthogonal Matching Pursuit. *IEEE Trans. Inf. Theory* **2007**, *53*, 4655–4666.
19. Tu, H., Bu, W., Wang, W., Gao, B., Feng, H., Wu, S. Applicability of Hadamard relaxation method to MMW and THz Imaging with compressive sensing. *Sig. Image Video Proc.* **2017**, *11*, 399–406.
20. Tan, X., Roberts, W., Li, J., Stoica, P. Sparse Learning Via Iterative Minimization With Application To Mimo Radar Imaging. *IEEE Trans. Signal Proc.* **2011**, *59*, 1088–1101.
21. Li, C.B., Yin, W.T., Jiang, H., Zhang, Y. An Efficient Augmented Lagrangian Method with Applications to Total Variation Minimization. *Comput. Optim. Appl.* **2013** *56*, 507–530.
22. Gopalsami, N., Liao, S.L., Elmer, T.W., Koehl, E.R., Heifetz, A., Raptis,A.C., Spinoulas, L., Katsaggelos, A.K. Passive Millimeterwave Imaging with Compressive Sensing. *Opt. Eng.* **2012**, *51*, 091614-091622.